

1                   **Seismic attenuation extraction from traffic signals**  
2                   **recorded by a single seismic station**

3                   **Yumin Zhao<sup>1</sup>, Enhedelihai Alex Nilot<sup>1</sup>, Bei Li<sup>1</sup>, Gang Fang<sup>1</sup>, Yunyue Elita Li<sup>2</sup>,**  
4                   **Wei Luo<sup>3</sup>**

5                   <sup>1</sup>Department of Civil and Environmental Engineering, National University of Singapore

6                   <sup>2</sup>Department of Earth, Atmospheric, and Planetary Sciences, Purdue University

7                   <sup>3</sup>Department of Geography, National University of Singapore

8                   **Key Points:**

- 9
- 10
- 11
- 12
- 13
- 14
- A new method is proposed for extracting seismic attenuation from moving vehicle sources recorded by a single seismic station.
  - We statistically resolve the daily seismic attenuation from hundreds of isolated traffic signals.
  - Variations in seismic attenuation highly correlate with rainfall, suggesting rainfall's causal effect through the groundwater system.

15 **Abstract**

16 Seismic ambient noise contains rich information about the physical properties of  
 17 the critical zone. From the motor vehicle noise, we extract the daily seismic attenuation  
 18 by quantifying the linear relationship between the frequency and amplitude ratio of paired  
 19 instantaneous spectra. After verifying the reliability of the proposed method, we apply  
 20 it to seismic ambient noise data collected at three urban sites. The estimated attenu-  
 21 ation is compared against three environmental variables: rainfall, temperature, and traf-  
 22 fic volume. The results show that the estimated seismic attenuation correlates most strongly  
 23 with precipitation with positive time lags, suggesting a high attenuation sensitivity to  
 24 changes in soil moisture and groundwater system. Furthermore, differences in attenuation-  
 25 precipitation correlations indicate that near-surface physical properties may vary signif-  
 26 icantly due to local site conditions. Our statistical method extracts reliable near-surface  
 27 information from highly complex urban ambient noise data, achieving unprecedented spa-  
 28 tial and temporal resolution compared to existing ambient noise imaging methods.

29 **Plain Language Summary**

30 Seismic waves travel through Earth's layers and contain information about the un-  
 31 derground physical properties. As the seismic waves travel longer distances, their am-  
 32 plitudes decay due to geometrical spreading and medium attenuation, the latter of which  
 33 could change rapidly due to changes in subsurface compaction and pore fluid saturation.  
 34 By measuring the seismic amplitude differences between waves emitted from the same  
 35 motor vehicle at two different locations, we estimate daily seismic attenuation statisti-  
 36 cally from hundreds of isolated traffic signals recorded by a single seismic sensor. By com-  
 37 paring the estimated time-varying seismic attenuation with rainfall, temperature, and  
 38 traffic volume, we find that precipitation dominates the correlation, suggesting a causal  
 39 relation between rainfall and seismic attenuation through changes of soil moisture con-  
 40 tent and groundwater level fluctuations.

41 **1 Introduction**

42 Human activities, such as driving, walking, and running, generate seismic waves  
 43 propagating through the near-surface and have greatly enriched the energy of the seis-  
 44 mic wavefield in the near-surface. Previous studies extracted human activities above the  
 45 ground from the seismic ambient noise data, such as the number of runners passing a  
 46 park trail (Zhao et al., 2022) and motor vehicles passing a road (Li et al., 2020; Lind-  
 47 sley et al., 2020; Wang et al., 2021). In addition, seismic ambient noise data contains in-  
 48 formation about the subsurface and has been used to resolve the underground physical  
 49 properties. For example, seismic traffic signals have been used for near-surface imaging  
 50 (Nakata, 2016; Dou et al., 2017; Y. Zhang et al., 2019), fault imaging (Brenguier et al.,  
 51 2019), and shallow subsurface Q-value estimation (Meng et al., 2021).

52 The changes in the underground physical properties, such as fluid saturation and  
 53 pore pressure, often lead to temporal changes in the propagation property of seismic waves.  
 54 Hence, seismic velocity changes have been extracted from active and passive seismic data  
 55 to characterize the changes in the underground physical properties (Lecocq et al., 2017;  
 56 Clements & Denolle, 2018; Rodríguez Tribaldos & Ajo-Franklin, 2021; Suzuki et al., 2021).  
 57 Recently, seismic ambient noise imaging with coda wave interferometry has demonstrated  
 58 its remarkable capability to extract velocity changes as low as 0.02% at the basin scale  
 59 (Mao et al., 2022). Field studies estimate seasonal velocity changes on the order of 1%  
 60 (Voisin et al., 2016; Garambois et al., 2019; Rodríguez Tribaldos & Ajo-Franklin, 2021)  
 61 in the shallower subsurface (less than 10 meters). Despite this amazing resolution to the  
 62 minute velocity changes, these results manifest a low sensitivity of seismic *velocity* to the  
 63 near-surface changes. Furthermore, most of these results are observed by averaging am-

64 bient noise data over tens of days at low frequencies, which may not provide the needed  
 65 temporal and spatial resolution for active groundwater/infrastructure management and  
 66 intervention.

67 On the other hand, intrinsic seismic attenuation, which causes seismic amplitudes  
 68 to decay faster than geometrical spreading, has also been used to study the changes of  
 69 the subsurface conditions. Centroid frequency shift method (Quan & Harris, 1997) and  
 70 spectral ratio method (Schoenberger & Levin, 1978; Ganley & Kanasewich, 1980; Hauge,  
 71 1981) are two commonly used methods to resolve seismic attenuation. Zhu et al. (2017)  
 72 estimated the spatiotemporal variations of seismic attenuation caused by CO<sub>2</sub> seque-  
 73 stration from the active seismic data with the centroid frequency shift method. The spec-  
 74 tral ratio method has been used to calculate the temporal changes in seismic attenua-  
 75 tion in the regions near earthquake faults and volcanoes (e.g., Chun et al., 2004; Titzschkau  
 76 et al., 2010; Kelly et al., 2013). Apart from the variations in seismic attenuation caused  
 77 by the underground changes, Tsuji et al. (2022) observed the correlation between the seis-  
 78 mic amplitude and atmosphere temperature that causes the change in thermal strains  
 79 near the ground surface. These findings suggest a higher sensitivity of seismic attenu-  
 80 ation to the near-surface changes. Nonetheless, existing studies on extracting seismic atten-  
 81 uation from ambient noise data are limited due to the high complexity and variabil-  
 82 ity of the ambient noise sources. To mitigate the unknown source problem, the conven-  
 83 tional ambient noise processing workflow relies heavily on normalization and long-time  
 84 averaging, which removes the amplitude information.

85 In this paper, we propose to first isolate individual motor vehicle signals, and then  
 86 estimate the shallow near-surface seismic attenuation with the spectral ratio method.  
 87 We select two amplitude spectra arriving at the same station at two different times from  
 88 the source. The logarithm of the amplitude ratio between each pair is a linear function  
 89 of frequency. The slope is expressed as a function of motor vehicle speed, surface wave  
 90 velocity, and the quality factor  $Q$ , which is used to quantify seismic attenuation. By es-  
 91 timating the slope measurements using data from hundreds of motor vehicles, we can  
 92 reasonably assume, on average, the motor vehicles travel at the speed limit of each road  
 93 and thereby remove their influence. Taking the low sensitivity of seismic velocity to near-  
 94 surface conditions into account, we convert the slope measurements into seismic atten-  
 95 uation estimates using a stationary surface wave velocity. We apply this method to both  
 96 synthetic examples and field noise data at three different sites. Comparing with rainfall,  
 97 temperature, and traffic volume, we find that the estimated time-varying seismic atten-  
 98 uation correlates most strongly with precipitation. Such a strong correlation with pos-  
 99 itive time lags suggests that changes in seismic attenuation are induced by rainfall through  
 100 changes in groundwater saturation and the soil's effective physical property.

## 101 2 Methodology

### 102 2.1 Traffic signal simulation

103 We assume a seismic sensor is deployed by the roadside, and a motor vehicle runs  
 104 towards the sensor and then drives off. The smallest distance between the motor vehi-  
 105 cle and the sensor is  $l$  (Figure 1a). At a given recording time  $t$ , the seismic sensor mea-  
 106 sures the cumulative waves emitted from the motor vehicle as a moving source at time  
 107  $\tau$ . At locations close to the road, seismic ambient noise is dominated by surface waves.  
 108 The measured amplitude decays with increasing vehicle-sensor distances because of ge-  
 109 ometrical spreading and seismic attenuation. We assume there are only fundamental mode  
 110 surface waves in the data, and the surface wave velocity is constant with respect to fre-  
 111 quencies above 10 Hz. Then the traffic signal recorded by the seismic sensor can be rep-  
 112 resented as:

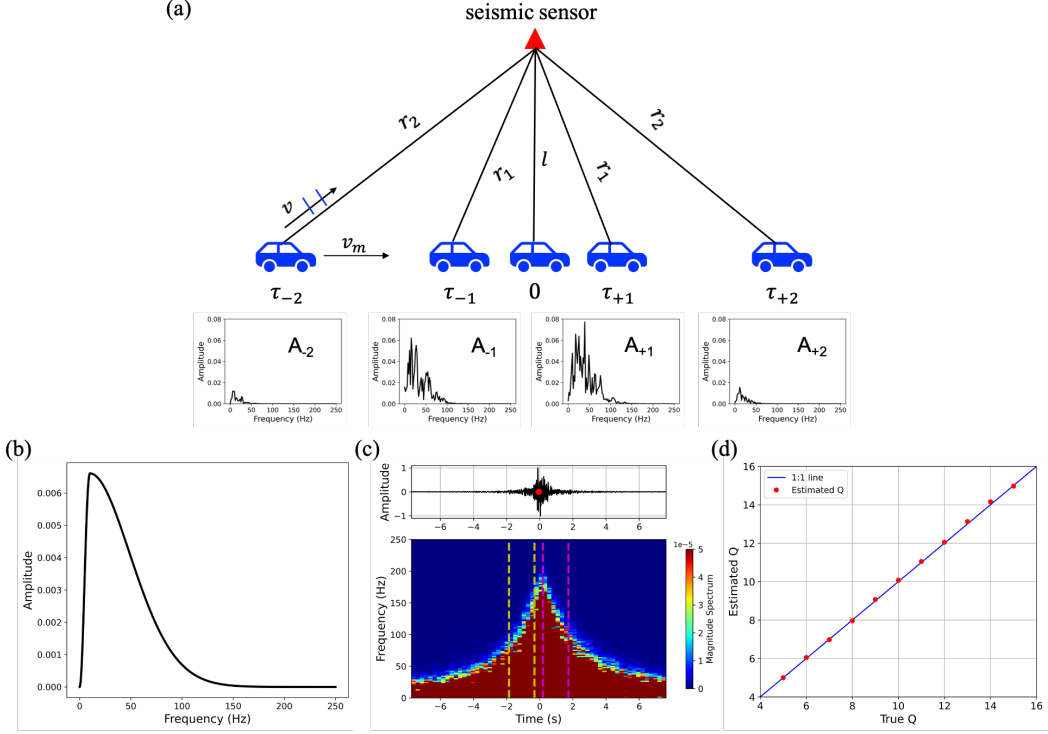


**Figure 1.** (a) Illustration of seismic traffic signal simulation. (b) Amplitude spectrum of the zero-phase source wavelet used to simulate the traffic signal. (c) Synthetic seismic data (upper) and its corresponding spectrogram (lower). The red dot in the upper panel marks the position of the peak, and the two yellow and two magenta dashed lines represent the two pairs of spectra selected for slope estimation. (d) Comparison between the reference  $Q$  values and the estimated ones.

$$d(\omega, t) = \int_{-\infty}^t \frac{S(\omega)\alpha(\tau)}{\sqrt{r(\tau)}} e^{-i\omega(\tau + \frac{r(\tau)}{v})} e^{i\omega(\ln(\frac{i\omega}{\omega_0}) \frac{r(\tau)}{\pi Q v})} d\tau, \quad (1)$$

where  $S(\omega)$  is the amplitude spectrum of the source wavelet,  $\alpha(\tau)$  denotes the road roughness factor and varies randomly with time  $\tau$ .  $r(\tau)$  is the distance between the motor vehicle and the seismic sensor at time  $\tau$ ,  $v$  is the surface waves velocity,  $\omega_0 = 2\pi f_0$  is the reference angular frequency,  $Q$  is the quality factor, and  $e^{i\omega(\ln(\frac{i\omega}{\omega_0}) \frac{r(\tau)}{\pi Q v})}$  is the attenuation term obtained based on the precise constant  $Q$  theory (Kjartansson, 1979). Assuming the motor vehicle arrives closest to the sensor at  $\tau = 0$ , the distance between the motor vehicle and the sensor at time  $\tau$  can be expressed as:

$$r(\tau) = \sqrt{l^2 + (v_m\tau)^2}, \quad (2)$$

where  $v_m$  is the speed of the motor vehicle.

## 2.2 Seismic attenuation estimation

Separating the amplitude and phase parts of Equation 1, we obtain

$$d(\omega, t) = \int_{-\infty}^t \frac{S(\omega)\alpha(\tau)}{\sqrt{r(\tau)}} e^{-\omega \frac{r(\tau)}{\pi Q v}} e^{-i\omega(\tau + \frac{r(\tau)}{v} - \ln(\frac{\omega}{\omega_0}) \frac{r(\tau)}{\pi Q v})} d\tau. \quad (3)$$

The recording time  $t$  and source excitation time  $\tau$  are not independent when a single source is considered. In fact,  $t = \tau + \frac{r(\tau)}{v}$ . When  $r(\tau)$  is small (i.e., sensor deployed close to the road) or  $v$  is large (i.e., ignoring the Doppler effect),  $t \approx \tau$ . Then we have

$$d(\omega, t) \approx \int_{-\infty}^t \frac{S(\omega)\alpha(t)}{\sqrt{r(t)}} e^{-\omega \frac{r(t)}{\pi Q v}} e^{-i\omega(t + \frac{r(t)}{v} - \ln(\frac{\omega}{\omega_0}) \frac{r(t)}{\pi Q v})} dt. \quad (4)$$

122 The instantaneous amplitude spectrum at time  $t$  is then obtained by taking the derivative  
123 of Equation 4 with respect to  $t$ :

$$\dot{d}(\omega, t) = \frac{S(\omega)\alpha(t)}{\sqrt{r(t)}} e^{-\omega \frac{r(t)}{\pi Q v}} e^{-i\omega(t + \frac{r(t)}{v} - \ln(\frac{\omega}{\omega_0}) \frac{r(t)}{\pi Q v})}. \quad (5)$$

We denote the amplitude spectra of the seismic data recorded at time  $\tau_{-1}$  and  $\tau_{-2}$  ( $\tau_{-1} < \tau_{-2} < 0$ ) as  $A_{-1}$  and  $A_{-2}$ , respectively (Figure 1a). These amplitudes are:

$$A_{-1} = |\dot{d}(\omega, \tau_{-1})| = \frac{S(\omega)\alpha(\tau_{-1})}{\sqrt{r(\tau_{-1})}} e^{-\omega \frac{r(\tau_{-1})}{\pi Q v}}, \quad (6)$$

and

$$A_{-2} = |\dot{d}(\omega, \tau_{-2})| = \frac{S(\omega)\alpha(\tau_{-2})}{\sqrt{r(\tau_{-2})}} e^{-\omega \frac{r(\tau_{-2})}{\pi Q v}}, \quad (7)$$

and their spectral ratio is

$$\frac{A_{-1}}{A_{-2}} = \frac{\alpha(\tau_{-1})\sqrt{r(\tau_{-2})}}{\alpha(\tau_{-2})\sqrt{r(\tau_{-1})}} e^{-\omega \frac{r(\tau_{-1}) - r(\tau_{-2})}{2Qv}}. \quad (8)$$

124 Taking the natural logarithm on both sides of Equation 8, we obtain

$$\ln\left(\frac{A_{-1}}{A_{-2}}\right) = c_1 - \frac{\pi(r(\tau_{-2}) - r(\tau_{-1}))}{Qv} f, \quad (9)$$

125 where  $c_1 = \ln\left(\frac{\alpha(\tau_{-1})\sqrt{r(\tau_{-2})}}{\alpha(\tau_{-2})\sqrt{r(\tau_{-1})}}\right)$ , and  $f = \frac{\omega}{2\pi}$ . Equation 9 is consistent with the spectral  
126 ratio method (Schoenberger & Levin, 1978; Ganley & Kanasewich, 1980; Hauge, 1981).

Similarly, for the seismic wave recorded at time  $\tau_{+1}$  and  $\tau_{+2}$  ( $0 < \tau_{+1} < \tau_{+2}$ ), we have

$$\ln\left(\frac{A_{+1}}{A_{+2}}\right) = c_2 - \frac{\pi(r(\tau_{+2}) - r(\tau_{+1}))}{Qv} f, \quad (10)$$

127 where  $c_2 = \ln\left(\frac{\alpha(\tau_{+1})\sqrt{r(\tau_{+2})}}{\alpha(\tau_{+2})\sqrt{r(\tau_{+1})}}\right)$ ,  $A_{+1}$  and  $A_{+2}$  are the amplitude spectra of the seismic  
128 wavelet recorded at time  $\tau_{+1}$  and  $\tau_{+2}$ , respectively. Equations 9 and 10 demonstrate the  
129 linear relationship between the logarithm of the spectral ratio and the frequency. Let  $\tau_{-1} =$   
130  $-\tau_1$ ,  $\tau_{-2} = -\tau_2$ ,  $\tau_{+1} = \tau_1$  and  $\tau_{+2} = \tau_2$ , where  $\tau_1$  and  $\tau_2$  are positive time constants.  
131 Then the same slope  $k = \frac{\pi(r(\tau_{+2}) - r(\tau_{+1}))}{Qv}$  can be estimated from these two equations.  
132 Keeping  $\tau_1$  and  $\tau_2$  fixed, we estimate the slope  $k$  statistically from traffic signals gener-  
133 ated by hundreds of motor vehicles over a few days. Hence, the vehicle speeds are as-  
134 sumed to be the speed limit of each road upon this averaging effect. Furthermore, since  
135 variations of surface wave velocity at shallow near-surface are at most on the order of  
136 1% (Voisin et al., 2016; Garambois et al., 2019; Rodríguez Tribaldos & Ajo-Franklin, 2021),  
137 the error in the estimated seismic attenuation caused by velocity variation would also  
138 be on the order of 1%. Finally, we convert the slope measurements to attenuation es-  
139 timates:

$$Q^{-1} = \frac{kv}{\pi(r(\tau_{\pm 2}) - r(\tau_{\pm 1}))}. \quad (11)$$

140 **3 Synthetic data examples**

141 We assume the minimum motor-vehicle-sensor distance is 1 m, the sampling fre-  
 142 quency is 500 Hz, and the recording period is 16 s. We set the surface wave velocity, mo-  
 143 tor vehicle speed, and the quality factor as  $v=150 \text{ m/s}$ ,  $v_m=50 \text{ km/h}$ , and  $Q=10$ , respec-  
 144 tively. Figure 1b shows the source wavelet we use to simulate the traffic signal. It is a  
 145 zero-phase source wavelet with a peak frequency of 10 Hz, which is given according to  
 146 the traffic signal recorded in the field. Its energy is mainly concentrated at lower frequen-  
 147 cies, and the high-frequency components present long-tail characteristics. Figure 1c shows  
 148 the synthetic seismic data and its corresponding spectrogram, which is obtained by ap-  
 149 plying a fast Fourier transform on the data with a sliding window of 0.256 s with 0.128  
 150 s overlap. We first identify the peak in the traffic signal, which is generated when the  
 151 motor vehicle is the closest to the sensor. Then we choose two pairs of amplitude spec-  
 152 tra at the time before and after the peak occurs (Figure 1d). In this example,  $\tau_1$  and  $\tau_2$   
 153 are 0.256 s and 1.792 s, respectively. Sampling  $Q$  between 5 and 15, we simulate the cor-  
 154 responding seismic data, estimate the quality factor  $Q$ , and compare them with the ref-  
 155 erence values in Figure 1d, which shows an excellent agreement.

156 As field data are always contaminated with noises, we conduct multiple synthetic  
 157 tests to demonstrate the reliability of the estimated slopes from seismic data with dif-  
 158 ferent signal-to-noise ratios (SNRs). The background noise (Figure S1 in the sup-  
 159 porting information), selected from field data recorded at three sites, was mainly generated  
 160 from the traffic noise on the nearby road. The noise presents strong energies at lower fre-  
 161 quencies while weak energy at higher frequencies, which could be caused by a combi-  
 162 nation of the source signature and attenuation. At highway and park sites, we observe strong  
 163 single-frequency noise at several frequencies caused by power transmission, construction,  
 164 and machinery. The surface waves velocities at the NUS exit and park sites are given  
 165 according to the dispersion curves at higher frequencies ( $>10 \text{ Hz}$ ) resolved by Niu et al.  
 166 (2022), which are about 180 m/s and 120 m/s, respectively. The underground condi-  
 167 tion at the highway site is similar to the NUS site, so the surface wave velocity is also  
 168 estimated at 180 m/s. Motor vehicle speeds at the three sites are given according to the  
 169 speed limits of the corresponding road, which are 40 km/h and 50 km/h, and 70 km/h,  
 170 respectively. The smallest distances between the motor vehicle for the NUS exit and high-  
 171 way sites are 1 m, while that for the park site is 7 m. The other parameters are the same  
 172 as those given in the synthetic example in Figure 1b-1d. We first simulate one clean data  
 173 for each site and then add different amounts of noise extracted from the corresponding  
 174 site. Finally, we obtain four datasets with different SNRs for each site: clean data, and  
 175 data with an SNR of 10, 5, and 1. The frequency band with a consistent slope is nar-  
 176 rrower when the SNR is lower (Figure S2 in the supporting information). Table S1 in the  
 177 supporting information summarizes the estimated slopes, the reference slopes, and the  
 178 estimation error for each case. For all three sites, the estimation error increases with SNR  
 179 decreases. Therefore, we use different frequency bands and different SNRs to filter the  
 180 chosen traffic signals at each site.

181 **4 Field data results**

182 The field data were collected at three sites: NUS exit, West Coast Highway road-  
 183 side, and by a trail in the West Coast Park. The recording is from early April to late  
 184 October 2020. The seismic sensor used to record the seismic ambient noise data is a three-  
 185 component SmartSolo IGU-16HR with a 5 Hz corner frequency. It was buried 10 cm be-  
 186 low the soil at each site. More information about these sites can be found in Li et al. (2020),  
 187 Fang et al. (2021), and Zhao et al. (2022). In this study, we only analyze the vertical com-  
 188 ponent recordings as they present the most consistent measurements with continuous de-  
 189 ployments. Figures S3a-S3c in the supporting information show 1-minute ambient noise  
 190 data recorded at the NUS exit, highway, and park site, respectively. The energy (red curve)  
 191 of the traffic signals recorded at the highway site is the highest, while that at the park

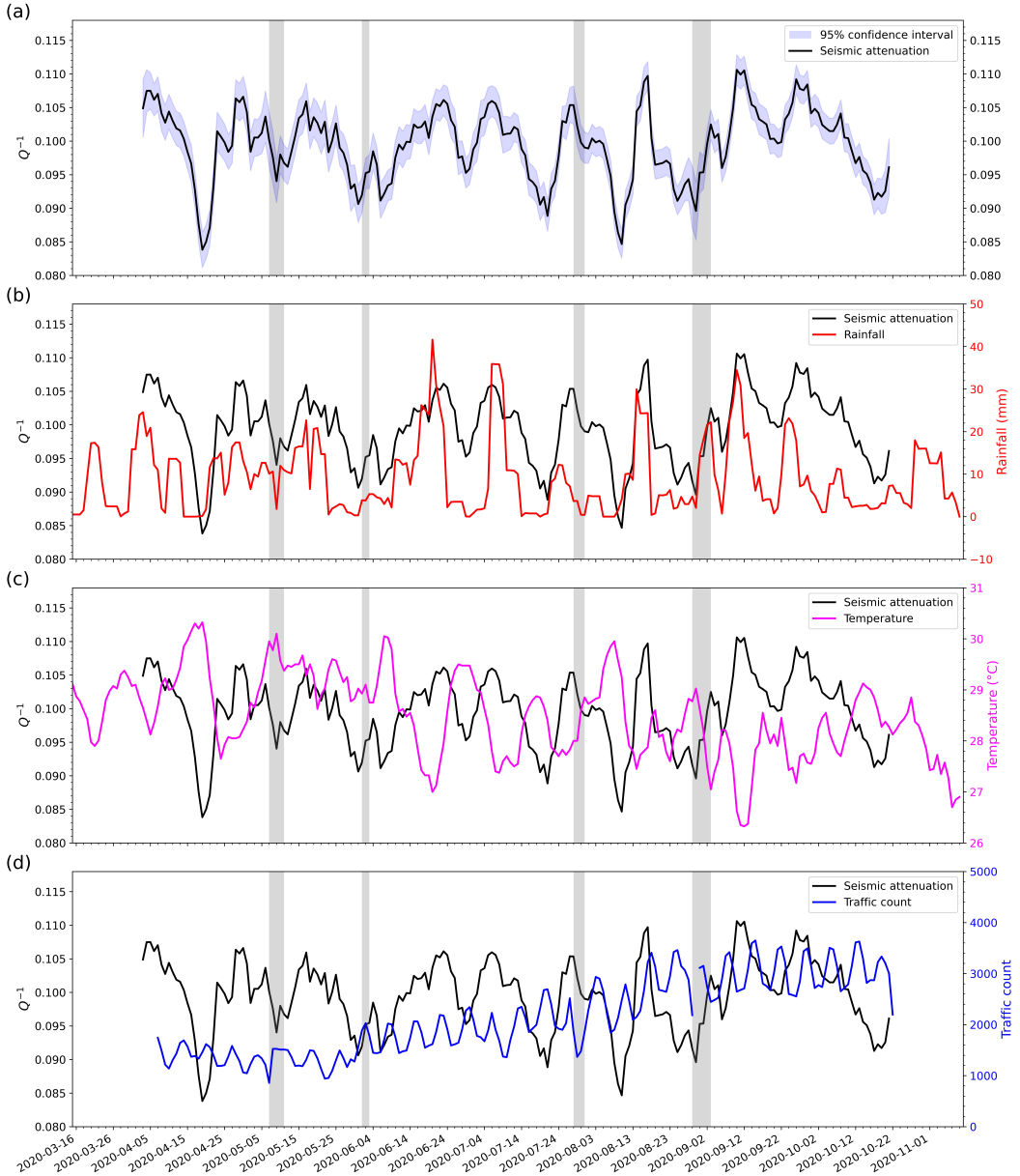


**Figure 2.** (a) Daily seismic attenuation estimated from the seismic ambient noise recorded at the NUS exit. The light blue shaded areas represent the 95% confidence interval of the estimated seismic attenuation. Comparison between daily seismic attenuation and (b) smoothed daily rainfall, (c) smoothed daily temperature, and (d) smoothed daily traffic count. The gray shaded areas denote the dates when the seismic ambient noise data was not collected.

site is the lowest. We can easily observe the coherent high-frequency ( $>100$  Hz) traffic signals at the NUS exit and highway sites. However, those recorded at the park site are severely attenuated. The high-frequency data at the highway site are further contaminated by the loud engine noise from various motor vehicles.

We identify individual vehicles from data recorded from 7:00 pm to 7:00 am the next day (local time) since the traffic is lighter and the background noise is weaker than that in the daytime. The daily seismic attenuation is estimated within a four-day long,

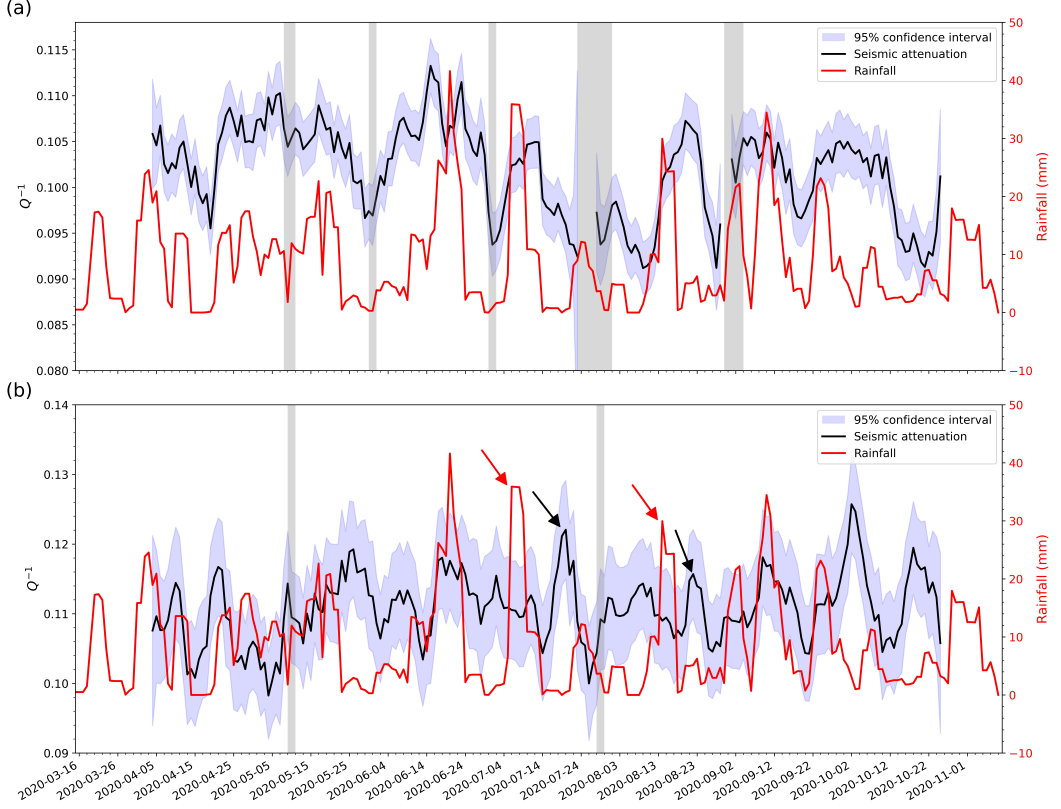


**Figure 3.** Comparison between the smoothed daily rainfall with the daily seismic attenuation estimated from the seismic ambient noise recorded at (a) West Coast Highway and (b) West Coast Park. The light blue shaded areas represent the 95% confidence interval of the estimated seismic attenuation. The gray shaded areas denote the dates when the seismic ambient noise data was not collected.

one-day sliding window. The four-day-long window length is selected after observing the four-day periodicity of the rainfall data. To be consistent, we also apply the same four-day-long, one-day moving window average to all environmental factors (rainfall, temperature, and traffic volume). Based on the data quality, the frequency bands we select to estimate the seismic attenuation from the data recorded at the NUS exit, highway, and park sites are 10-80 Hz and 10-60 Hz, and 10-40 Hz, respectively. We summarize the site parameters in the first columns of Table 1. Further details of the processing procedure are given in the supporting information.

**Table 1.** Site parameters and Q ranges

Site	v (m/s)	$v_m$ (km/h)	$l$ (m)	Freq. Band (Hz)	Depth Range (m)	Q Range
NUS exit	180	40	1	10 - 80	0.75 - 6	9.0 - 11.9
West Coast Highway	180	70	1	10 - 60	1 - 6	8.9 - 11.0
West Coast Park	120	50	7	10 - 40	1 - 4	7.9 - 10.2

**Table 2.** Maximum correlation coefficients and corresponding time lags (in days) between the estimated Q and three potential factors.

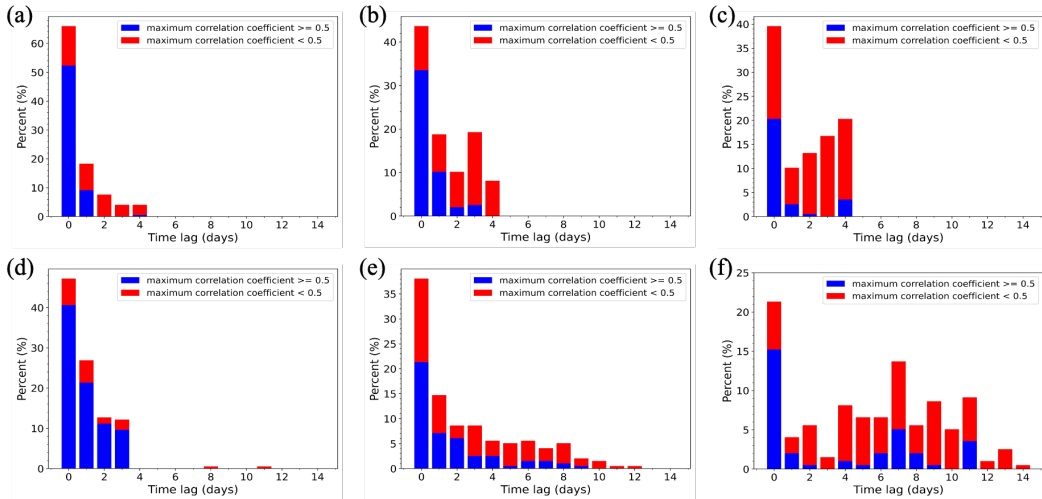
Factor \ Site	NUS exit		West Coast Highway		West Coast Park	
	CC	Time lag (day)	CC	Time lag (day)	CC	Time lag (day)
Rainfall	0.60	1	0.53	3	0.25	9
Temperature	-0.62	1	-0.50	1	-0.24	28
Traffic Count	0.19	11	0.22	98	0.32	0

Figure 2a displays the daily mean seismic attenuation, and its 95% confidence interval (CI) estimated from the seismic ambient noise recorded at the NUS exit. We estimate the 95% CI by adding and subtracting the corresponding margin of error from the sample mean (Zar, 1999; Seabold & Perktold, 2010). The narrow CI (Figure 2a) indicates the small uncertainty of our estimation. Figures 2b-2d show the comparison between the estimated seismic attenuation and daily rainfall, temperature, and traffic count, respectively. We observe the periodical changes in the rainfall and temperature data, which can also be observed in the estimated seismic attenuation with strong positive and negative correlations, respectively (Figures 2b and 2c). The maximum correlation coefficients (CC) between attenuation and rainfall, and temperature are 0.60 and -0.62, with the corresponding time lags both at one day, respectively (Table 2). These results show that changes of seismic attenuation occur on average one day after rainfall and temperature changes. These strong correlations and positive time lags have a strong indication of the causal effects of both rainfall and temperature on seismic attenuation. However, temperature changes in tropical regions are strongly regulated by rainfall, as these two environmental variables have a large CC at -0.65 with a time lag of 0. Moreover, air temperature remained at a high level with small variations ( $28.5^{\circ} \pm 1^{\circ}$  C). Therefore, we expect a smaller direct causal contribution of temperature to the subsurface physical properties. Meanwhile, there is no obvious correlation between attenuation and traffic volume (Figure 2d and Table 2), suggesting a stable pavement condition throughout the monitoring period. Based on these observations, we focus the results at the other two sites on the correlation analysis between attenuation and rainfall within the main body of the paper and refer the readers to the supplementary material for comparisons with other environmental factors.

At the highway site (Figure 3a), we observe similar correlation patterns between attenuation and rainfall as at the NUS exit. This is expected since the sensors are deployed within 1 m from the pavements. The road bases, although one for a local road (NUS exit) and the other for a highway (West Coast Highway), are constructed according to similar engineering standards (LTA, 2017), and hence behave similarly in response to the environment.

In contrast, the correlation patterns at the park site are significantly different (Figure 3b). The overall CCs between attenuation and all three potential factors are small (Table 2), while Figure 3b shows that the time lags between the estimated seismic attenuation and rainfall may vary over time. If it rains after a long drought (about 15 days), the time lag between the rainfall and estimated seismic attenuation is small. If the second rain event happens within a week from a previous rainfall, the time lag is much larger (red and black arrows). These phenomena indicate that the site condition at the West Coast Park is significantly different from the two roadside sites, where the attenuation-rainfall correlation is mostly stationary and synchronized.

To better analyze the temporal stationarity of the attenuation-rainfall correlation, we calculate the local cross-correlations between the two time series with sliding win-



**Figure 4.** Histogram of time lags corresponding to the maximum local cross-correlation between attenuation and rainfall with a sliding window of 5 days (Top row) and of 15 days (Bottom row). (a) and (d): NUS exit; (b) and (e): West Coast Highway; (c) and (f): West Coast Park.

248       dows of 5 days and 15 days for all three sites (Figures S4-S6 in the supporting information)  
249       with the focus on the maximum correlation lags. We show the corresponding histograms  
250       of the local time lag in Figure 4. We assume when the local maximum CC is  
251       greater than 0.5, the measured lag is more trustworthy, and color-code the histograms  
252       accordingly (blue for  $CC \geq 0.5$ , and red otherwise). At all sites and with both window  
253       lengths, we observe a dominant mode at the time lag = 0 day. This indicates a fast re-  
254       sponse mechanism of the near-surface physical property to rainfall, which effectively reaches  
255       equilibrium within one day. Comparing the results from two different window lengths,  
256       the time lag distributions do not change significantly at the NUS exit (Figures 4a and 4b)  
257       and the West Coast Highway (Figures 4d and 4e), further demonstrating the temporal  
258       stationarity of the attenuation-rainfall correlation. A striking contrast is illustrated when  
259       comparing Figures 4c and 4f for the West Coast Park site, where a second mode at the  
260       time lag = 7 days shows up when the window length increases to 15 days. This bimodal  
261       feature highlights the nonstationarity of the attenuation-rainfall correlation, suggesting  
262       a more complex site condition.

## 263       5 Discussions

264       Near-surface soil and rock formations react to environmental variations and human  
265       activities above the Earth's surface. One of the most direct reactions happens during rain-  
266       water infiltration into the groundwater aquifer (Martini et al., 2009). Meanwhile, near-  
267       surface soil also releases water back to the surface through discharge and evaporation,  
268       which forms the loop between the surface water and groundwater system (Brouwer et  
269       al., 1985). Situated in the tropical region, Singapore receives a large amount of rainfall  
270       throughout the year. The top of the water table depth sits at 1-3 m (W. Zhang et al.,  
271       2018), which is within the visible depth ranges of surface waves at all three sites (Ta-  
272       ble 1). Integrating all information, the strong correlation between attenuation and rain-  
273       fall, as well as the positive time lags, suggest that the measured attenuation changes are  
274       likely the results of the tropical rain events through the groundwater system, which reg-  
275       ulates the time response differently due to different site conditions.

We sample two types of urban sites: the engineered road base and the public lawn managed by the municipal. Anticipating heavy tropical downpours in Singapore, the infiltration rate of the sublayer pavement is designed to be at least 50 mm/hour (LTA, 2017; Fwa et al., 2015), and the pavement drainage system is well-developed (PUB & IES, 2013; PUB, 2018). When there is no rain, near-surface soil moisture evaporates on a similar time scale. Therefore, at the two roadside locations, we observe a nearly instantaneous response of the groundwater to the rainwater, as manifested by the 0-day time lag between the attenuation-rainfall correlation. For the park site, at the beginning of the rainy period, the infiltration rate of the dry soil can also be relatively high, the rainwater quickly seeps into the ground, and attenuation responds rapidly (the 0-day mode). With continuous rainfall, the near-surface soil retains a large amount of water, decreasing the infiltration rate (Brouwer et al., 1985). Furthermore, moisture and water in the lawn soil evaporate slowly due to dense vegetation and shading. Therefore, in these cases, it takes longer for the rainwater to seep into the ground (the 7-day mode). Such detailed analysis of the bimodal behavior of attenuation-rainfall correlation could provide important insights into the surface water-groundwater system and better guidance for irrigation and groundwater management. Table 1 shows the site parameters and the estimated Q ranges of all three sites. The Q value spans similar ranges for the two roadside sites, but it is smaller at the park site, as expected according to the site conditions. These site-dependent differences not only demonstrate the applicability of our attenuation estimation method but also provide future references to attenuation interpretation for different site conditions.

To convert the slope measurements to attenuation estimates, we make explicit assumptions about the vehicle speed and seismic velocities. The constant vehicle speed assumption and the nondispersive, stationary seismic velocity assumption are both reasonable for the sites investigated in this paper. Nonetheless, these parameters can be measured using additional sensors such as speed cameras and an array of seismometers. Adding more sensors will certainly increase the deployment and computational cost, but it could potentially further increase the temporal resolution as it eliminates the need for statistical averaging. Nonetheless, this study has already demonstrated a steep increase in temporal resolution from months to days, which could have a significant impact on the real-time monitoring of near-surface infrastructure, irrigation, and groundwater management. Our method relies on the accurate measurements of high-frequency ambient seismic data. The raw data volume is large. However, by extracting the isolated traffic signals at night (7:00 pm-7:00 am) and utilizing the amplitude spectral information, our workflow can be effectively adapted to streamed data for block or batch processing with high computational efficiency.

## 6 Conclusions

We statistically extract daily seismic attenuation from hundreds of isolated traffic signals and observe a strong attenuation-rainfall correlation. The results suggest that the variations in seismic attenuation are mainly caused by groundwater changes resulting from the recharge of rainfall. The time lags maximizing local windowed cross-correlations are site-dependent, revealing the differences in the temporal stationarity of the attenuation-rainfall correlation. Such detailed analysis could provide important insights into the surface water-groundwater system and better guidance for infrastructure monitoring, irrigation, and groundwater management. This study demonstrates that rich information in the urban seismic ambient noise can be distilled by combining geophysics and applied data science.

324 **7 Open Research**

325 Seismic data and the associate codes used in this study are available and can be  
 326 downloaded from the following links. NUS exit: <https://doi.org/10.5281/zenodo.7494032>.  
 327 West Coast Highway: <https://doi.org/10.5281/zenodo.7494035>. West Coast Park:  
 328 <https://doi.org/10.5281/zenodo.7494036>. The rainfall and temperature data are  
 329 downloaded from the website of Meteorological Service Singapore (<http://www.weather.gov.sg/climate-historical-daily/>). Supporting information for this article includes  
 330 the processing procedure, six figures, and one table. The website was last accessed in Novem-  
 331 ber 2022.  
 332

333 **Acknowledgment**

334 The authors acknowledge Cambridge Sensing Pte Ltd. for the financial support.  
 335 We thank Yuxuan Zhou and Zhaoxin Liu for the discussion. We thank Dr. Sjoerd de Rid-  
 336 der and an anonymous reviewer for their constructive suggestions, which have been very  
 337 useful in improving the article.

338 **References**

- 339 Brenguier, F., Boué, P., Ben-Zion, Y., Vernon, F., Johnson, C., Mordret, A., ... oth-  
 340     ers (2019). Train traffic as a powerful noise source for monitoring active faults  
 341     with seismic interferometry. *Geophysical Research Letters*, *46*(16), 9529–9536.
- 342 Brouwer, C., Goffeau, A., & Heibloem, M. (1985). Irrigation Water Management:  
 343     Training manual no. 1-Introduction into Irrigation. Food and Agriculture  
 344     Organization of the United Nations. *Land and Water Development Division*.
- 345 Chun, K.-Y., Henderson, G. A., & Liu, J. (2004). Temporal changes in P wave at-  
 346     tenuation in the Loma Prieta rupture zone. *Journal of Geophysical Research:*  
 347     *Solid Earth*, *109*(B2).
- 348 Clements, T., & Denolle, M. A. (2018). Tracking groundwater levels using the ambi-  
 349     ent seismic field. *Geophysical Research Letters*, *45*(13), 6459–6465.
- 350 Dou, S., Lindsey, N., Wagner, A. M., Daley, T. M., Freifeld, B., Robertson, M., ...  
 351     Ajo-Franklin, J. B. (2017). Distributed acoustic sensing for seismic monitoring  
 352     of the near surface: A traffic-noise interferometry case study. *Scientific reports*,  
 353     *7*(1), 1–12.
- 354 Fang, G., Elita Li, Y., Nilot, E., Zhao, Y., & Cheng, A. (2021). Anonymous vehicle  
 355     identification on seismic spectrograms. In *First international meeting for ap-*  
 356     *plied geoscience & energy* (pp. 1886–1890).
- 357 Fwa, T., Lim, E., & Tan, K. (2015). Comparison of permeability and clogging char-  
 358     acteristics of porous asphalt and pervious concrete pavement materials. *Trans-*  
 359     *portation Research Record*, *2511*(1), 72–80.
- 360 Ganley, D., & Kanasewich, E. (1980). Measurement of absorption and disper-  
 361     sion from check shot surveys. *Journal of Geophysical Research: Solid Earth*,  
 362     *85*(B10), 5219–5226.
- 363 Garambois, S., Voisin, C., Romero Guzman, M., Brito, D., Guillier, B., & Réfloch,  
 364     A. (2019). Analysis of ballistic waves in seismic noise monitoring of water table  
 365     variations in a water field site: added value from numerical modelling to data  
 366     understanding. *Geophysical Journal International*, *219*(3), 1636–1647.
- 367 Hauge, P. S. (1981). Measurements of attenuation from vertical seismic profiles.  
 368     *Geophysics*, *46*(11), 1548–1558.
- 369 Kelly, C., Rietbroek, A., Faulkner, D., & Nadeau, R. (2013). Temporal changes  
 370     in attenuation associated with the 2004 M6.0 Parkfield earthquake. *Journal of*  
 371     *Geophysical Research: Solid Earth*, *118*(2), 630–645.
- 372 Kjartansson, E. (1979). Constant Q-wave propagation and attenuation. *Journal of*  
 373     *Geophysical Research: Solid Earth*, *84*(B9), 4737–4748.

- 374 Lecocq, T., Longuevergne, L., Pedersen, H. A., Brenguier, F., & Stammmer, K.  
 375 (2017). Monitoring ground water storage at mesoscale using seismic noise:  
 376 30 years of continuous observation and thermo-elastic and hydrological model-  
 377 ing. *Scientific reports*, 7(1), 1–16.
- 378 Li, Y. E., Nilot, E., Zhao, Y., & Fang, G. (2020). Seismology for urban activity  
 379 monitoring in Singapore under the impact of COVID-19.  
 380 doi: <https://doi.org/10.31219/osf.io/tvj2w>.
- 381 Lindsey, N. J., Yuan, S., Lellouch, A., Gualtieri, L., Lecocq, T., & Biondi, B. (2020).  
 382 City-scale dark fiber DAS measurements of infrastructure use during the  
 383 COVID-19 pandemic. *Geophysical research letters*, 47(16), e2020GL089931.
- 384 LTA. (2017). Standard details of road elements. *Singapore, 2017*.
- 385 Mao, S., Lecointre, A., van der Hilst, R. D., & Campillo, M. (2022). Space-time  
 386 monitoring of groundwater fluctuations with passive seismic interferometry.  
 387 *Nature communications*, 13(1), 1–9.
- 388 Martini, F., Bean, C. J., Saccorotti, G., Viveiros, F., & Wallenstein, N. (2009).  
 389 Seasonal cycles of seismic velocity variations detected using coda wave inter-  
 390 ferometry at Fogo volcano, São Miguel, Azores, during 2003–2004. *Journal of*  
 391 *Volcanology and Geothermal Research*, 181(3-4), 231–246.
- 392 Meng, H., Ben-Zion, Y., & Johnson, C. W. (2021). Analysis of seismic signals gen-  
 393 erated by vehicle traffic with application to derivation of subsurface Q-values.  
 394 *Seismological Society of America*, 92(4), 2354–2363.
- 395 Nakata, N. (2016). Near-surface S-wave velocities estimated from traffic-induced  
 396 Love waves using seismic interferometry with double beamforming. *Interpreta-  
 397 tion*, 4(4), SQ23–SQ31.
- 398 Niu, Y., Li, Y. E., Chian, S. C., Nilot, E., & Fang, G. (2022). In-situ physical prop-  
 399 erties of reclaimed lands in Singapore. *The Leading Edge*, 41(5), 296–303.
- 400 PUB. (2018). Active, Beautiful, Clean Waters Design Guidelines 4<sup>th</sup> Edition. *Singa-  
 401 pore, 2018*.
- 402 PUB, & IES. (2013). Managing Urban Runoff - Drainage Handbook 1<sup>st</sup> edition. *Sin-  
 403 gapore, 2013*.
- 404 Quan, Y., & Harris, J. M. (1997). Seismic attenuation tomography using the fre-  
 405 quency shift method. *Geophysics*, 62(3), 895–905.
- 406 Rodríguez Tribaldos, V., & Ajo-Franklin, J. B. (2021). Aquifer monitoring using  
 407 ambient seismic noise recorded with distributed acoustic sensing (DAS) de-  
 408 ployed on dark fiber. *Journal of Geophysical Research: Solid Earth*, 126(4),  
 409 e2020JB021004.
- 410 Schoenberger, M., & Levin, F. (1978). Apparent attenuation due to intrabed multi-  
 411 ples, II. *Geophysics*, 43(4), 730–737.
- 412 Seabold, S., & Perktold, J. (2010). statsmodels: Econometric and statistical model-  
 413 ing with python. In *9th python in science conference*.
- 414 Suzuki, R., Yamaoka, K., Tsuji, S., & Watanabe, T. (2021). Ground water-induced  
 415 changes in velocities of P and S waves (Vp and Vs) measured using an accu-  
 416 rately controlled seismic source. *Earth, Planets and Space*, 73(1), 1–12.
- 417 Titzschkau, T., Savage, M., & Hurst, T. (2010). Changes in attenuation related to  
 418 eruptions of Mt. Ruapehu Volcano, New Zealand. *Journal of Volcanology and*  
 419 *Geothermal Research*, 190(1-2), 168–178.
- 420 Tsuji, S., Yamaoka, K., & Ikuta, R. (2022). Temporal change in seismic wave atten-  
 421 uation using highly stable vibration sources. *Earth, Planets and Space*, 74(1),  
 422 1–19.
- 423 Voisin, C., Garambois, S., Massey, C., & Brossier, R. (2016). Seismic noise monitor-  
 424 ing of the water table in a deep-seated, slow-moving landslide. *Interpretation*,  
 425 4(3), SJ67–SJ76.
- 426 Wang, X., Zhan, Z., Williams, E. F., Herráez, M. G., Martins, H. F., & Karrenbach,  
 427 M. (2021). Ground vibrations recorded by fiber-optic cables reveal traffic  
 428 response to COVID-19 lockdown measures in Pasadena, California. *Communi-*

- cations Earth & Environment, 2(1), 1–9.

Zar, J. H. (1999). *Biostatistical analysis*. Pearson Education India.

Zhang, W., Wang, W., Zhou, D., Zhang, R., Goh, A. T. C., & Hou, Z. (2018). Influence of groundwater drawdown on excavation responses—A case history in Bukit Timah granitic residual soils. *Journal of Rock Mechanics and Geotechnical Engineering*, 10(5), 856–864.

Zhang, Y., Li, Y. E., Zhang, H., & Ku, T. (2019). Near-surface site investigation by seismic interferometry using urban traffic noise in Singapore. *Geophysics*, 84(2), B169–B180.

Zhao, Y., Li, Y. E., Nilot, E., & Fang, G. (2022). Urban Running Activity Detected Using a Seismic Sensor during COVID-19 Pandemic. *Seismological Society of America*, 93(1), 181–192.

Zhu, T., Ajo-Franklin, J. B., & Daley, T. M. (2017). Spatiotemporal changes of seismic attenuation caused by injected CO<sub>2</sub> at the Frio-II pilot site, Dayton, TX, USA. *Journal of Geophysical Research: Solid Earth*, 122(9), 7156–7171.